Reservoir-induced deformation and continental rheology in vicinity of Lake Mead, Nevada

Georg Kaufmann [1]

Research School of Earth Sciences, Australian National University, Canberra, Australia

Falk Amelung [2]

Department of Geophysics, Stanford University, Stanford, California

Abstract. Lake Mead is a large reservoir in Nevada, formed by the construction of the 221-m-high Hoover Dam in the Black Canyon of the Colorado River. The lake encompasses an area of 635 km^2, and the total volume of the reservoir is 35.5 km^3. Filling started in February 1935. On the basis of a first-order leveling in 1935, several levelings were carried out to measure the deformation induced by the load of the reservoir. Subsidence in the central parts of the lake relative to the first leveling was around 120 mm (1941), 218 mm (1950), and 200 mm (1963). The subsidence pattern clearly shows relaxation of the underlying basement due to the water load of the lake, which ceased after 1950. Modeling of the relaxation process by means of layered, viscoelastic, compressible flat Earth models with a detailed representation of the spatial and temporal distribution of the water load shows that the thickness of the elastic crust underneath Lake Mead is 30 ± 3 km. The data are also consistent with a 10-km-thick elastic upper crust and a 20-km-thick viscoelastic lower crust, with 10^{20} Pa s as a lower bound for its viscosity. The subcrust has an average viscosity of $10^{18\pm0.2}$ Pa s, a surprisingly low value. The leveling data constrain the viscosity profile down to ~200 km depth.

1. Introduction

The deformation of the Earth's crust and mantle in response to forces such as topographical and glacial loading is controlled by its rheological properties. It is well established that the response of the upper crust is elastic and that it may fail brittlely along faults during earthquakes and that the response of the mantle is distributed ductile flow (dislocation creep). Very little is certain about the rheology between upper crust and mantle.

Laboratory rock mechanics data, extrapolated to crustal depth, suggest that for continents a relatively strong upper crust is underlain by a relatively weak lower crust and a relatively strong uppermost mantle [e.g., *Goetze and Evans*, 1979; *Brace and Kohlstedt*, 1980; *Kohlstedt et al.*, 1995]. These so-called strength profiles are based on assumptions about crustal composition (quartz content), thermal structure, activation energy, and strain rate. Their applicability to the Earth's crust is debated.

Various types of field data exist to constrain the rheological properties of the Earth's crust and mantle. Observations of bending of the crust under topographical loads (see *Burov and Diament* [1995], for a review) and of the growth of topography by repeated earthquakes [*King et al.*, 1988; *Stein et al.*, 1988; *Armijo et al.*, 1996] provide information about the flexural rigidity of the mechanically competent crust. With several assumptions the flexural rigidity can be converted into an elastic crustal thickness. Observations of rebound induced by the melting of the large paleoice sheets provide information about the viscosity of the upper and lower mantle [e.g., *Lambeck et al.*, 1996; *Mitrovica*, 1996; *Mitrovica and Forte*, 1997; *Lambeck et al.*, 1998]. Few field data exist to constrain the rheological properties of the lower crust and of the uppermost mantle. The Earth's rheological structure at this depth cannot be resolved by large-scale glacial loads because the spatial and the temporal distribution of the icesheets is not well enough known. Sources of information for lower crustal and uppermost mantle rheology include the deformed paleoshorelines of Lake Bonneville, a Pleistocene glacial meltwater lake [e.g., *Passey*, 1981; *Nakiboglu and Lambeck*, 1982, 1983; *Bills and May*, 1987; *Bills et al.*, 1994] and uplift related to coalmining in NW Germany [*Klein et al.*, 1997].

The rheological properties of the lower crust and upper mantle in principle can also be constrained from observations of transient deformation after the loading of the crust by the sudden slip during an earthquake (postseismic de-

formation) [*Thatcher et al.*, 1980; *Thatcher,* 1983; *Taibai,* 1989; *Rydelek and Sacks,* 1990; *Pollitz and Sacks,* 1992; *Buergmann et al.,* 1997; *Pollitz et al.,* 1998]. The interpretation of these data in terms of rheological structure, however, can be ambiguous. The observed surface deformation not only represents relaxation of the ductile part of the lithosphere, it also depends on the amount and spatial distribution of afterslip that may occur on the earthquake fault or neighboring faults [*Buergmann et al.,* 1997]. Furthermore, the load (the earthquake slip distribution) may be poorly known. For strike-slip faults, surface deformation data inherently have limited resolving power for the mode of deformation beneath the seismogenic crust [*Savage,* 1990].

In this paper we present a new data set to constrain the rheological properties of the continental crust and of the uppermost mantle: historic geodetic leveling observations of the time-dependent deformation after filling of the Lake Mead Reservoir in Arizona and Nevada in 1935. It is actually an old data set, but its resolving power in terms of the crustal and mantle rheology has not been appreciated previously. Most of the data are published in a report by the U. S. Geological Survey (USGS) in 1960 [*Smith et al.,* 1960]. These data are of particular value because both the spatial scale of the load ($L < 50$ km) and the relaxation time ($T < 25$ years) are small in comparison to classical loading problems like the disappearance of Lake Bonneville ($L \simeq 300$ km, $T \simeq 5000$ years) or Late Pleistocene deglaciation ($L \simeq 200\text{-}2000$ km, $T \simeq 10{,}000\text{-}100{,}000$ years). The size of the Lake Mead load is of the same order as seismic loads, and the timescale of the observations is comparable to the timescale of postseismic relaxation data. The advantage of the Lake Mead load in contrast to seismic loads is that the size and the temporal evolution of the load are very well known. We show that the leveling data resolve the rheological structure of the crust and upper mantle in the Lake Mead region down to ~200 km depth.

We discuss several rheological models for the Lake Mead region by comparing the predicted to the observed deformation. Our Earth model is a layered, Maxwell-viscoelastic half-space. First, a forward modeling strategy is employed for simple two- and three-layer Earth models. The best fitting models are then refined with a nonlinear Tarantola-Valette inversion. This continuum model approach has its limitations because it does not account for movements along faults. The continuum models reproduce well the general deformation pattern, but individual section height differences may be less well reproduced.

2. Regional Setting

The Lake Mead Reservoir is located in the southeastern Basin and Range Province in the states of Nevada and Arizona, ~40 km of Las Vegas (Figure 1). The reservoir was formed by the construction of the Hoover Dam in 1935 in the Black Canyon of the Colorado River. The area has an average elevation around 1000 m. To the east, the Basin and Range Province gives way to the Colorado Plateau, with the Grand Wash Cliffs abruptly rising around 1000 m above
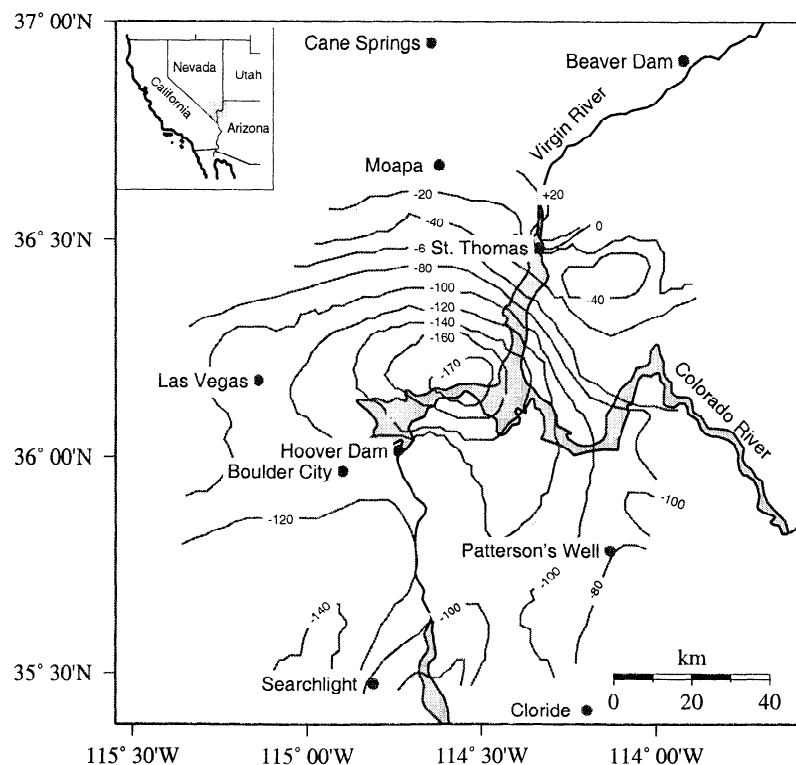

Figure 1. Lake Mead location map and relative subsidence between 1935 and 1950 (in mm), adopted from *Longwell* [1960a]. The basins are Boulder Basin (B), Virgin Basin (V), and Pierce Basin (P).

the lake. The Basin and Range Province is characterized by generally northward trending mountain ridges, intersected by wide basins with low relief. As a consequence, Lake Mead consists of wide and low-walled basins such as the Boulder, Virgin, and Pierce Basins and narrow, steep-walled flooded canyons [*Longwell*, 1960b]. The two largest basins, the Virgin and the Boulder Basins, account for 60% of the total water stored. Lake Mead extends $\sim$170 km upstream toward the Grand Canyon and $\sim$60 km up the Virgin River. The width varies from several hundred meters in the canyons to a maximum of 13 km. The reservoir covers $\sim$635 km^2 and has a maximum depth of 150 m and storage capacity of 35.5 km^3 of water.

The deformation caused by the load of the Lake Mead Reservoir is characterized by a nearly circular area of subsidence with an extent of 100 km (Figure 1) and maximum subsidence near the center of the lake. The leveling data (sections 3.2 and 3.3) show that subsidence was progressive for $\sim$15 years and had ceased $\sim$25 years after the filling of the lake [*Lara and Sanders*, 1970].

3. Observational Data

3.1. Lake Level Data

Hoover Dam was build between June 1933 and May 1935, and the lake started filling on February 1, 1935. In 1938,

three years after completion of the dam, the lake was filled to 75% of its maximum capacity. Since then, the lake is filled on average to $\sim$75% with yearly variations of up to 15%. For flood control purposes, on April 1 of each year the lake may be filled to no more than 70% [*Langbein*, 1960]. The seasonal variations of the Lake level are around 20%.

The water load varies with time and depends on the lake level. To derive a load model, we follow *Stanley* [1960] and divide the lake into nine different basins. Each basin is represented by several discs with fixed radii so that the surface area of a basin is reasonably approximated (Figure 2). The thickness of a disc varies with time, sampled at one year intervals. We do not account for seasonal variations of the load. For a given year the thickness h_{ij} of disc i in basin j is $h_{ij} = V_j / (\sum_i \pi r_{ij}^2)$, with r_{ij} the disc radius. The basin capacity V_j is taken from Stanley using the lake level data from *Langbein* [1960] averaged over 1 year. The effect of the variable basin capacity on the lake volume is illustrated in Figure 3. The maximum lake level variation between 1938 and 1950 is $\sim$15 m and corresponds to a change in water volume of $\sim$25%.

3.2. Leveling Data

During a leveling survey, relative height differences between adjacent points along the survey line are derived as section heights, dh_i. The topographical height H_i of the ith
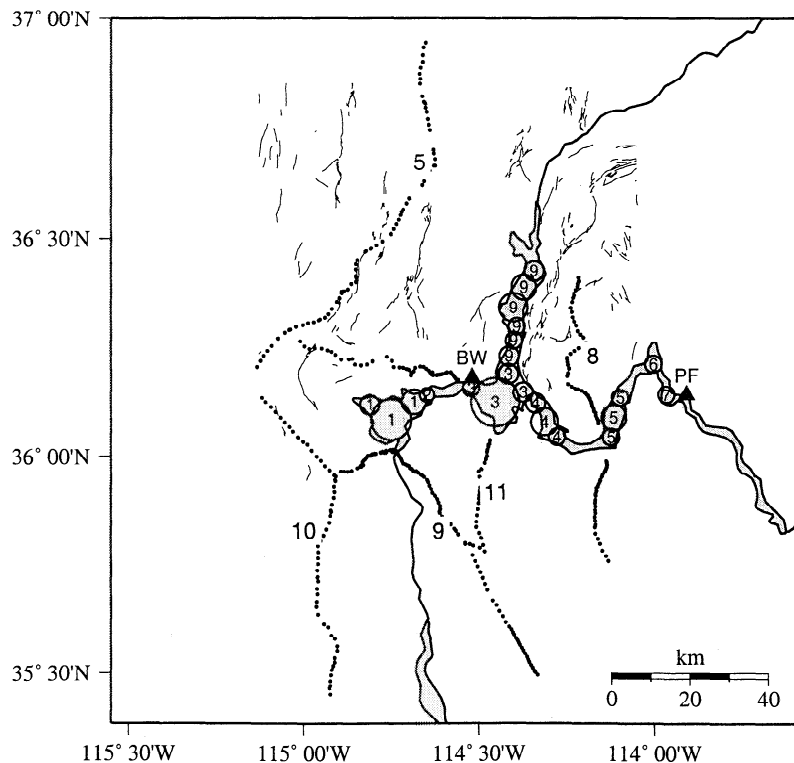

Figure 2. Survey stations (dots) of leveling lines used in this study and disc load approximation of the water load. The lake is divided into nine basins following *Stanley* [1960]; Boulder Basin (1), Boulder Canyon (2), Virgin Basin (3), Temple Bar Area (4), Gregg Basin (5), Grand Bay (6), Pierce Basin (7), Upper Granite Gorge (8, no disc load), and Overton Arm (9). Triangles indicate tide gage locations Boulder Wash (BW) and Pierce Ferry (PF). The thin lines are mapped faults within the region.
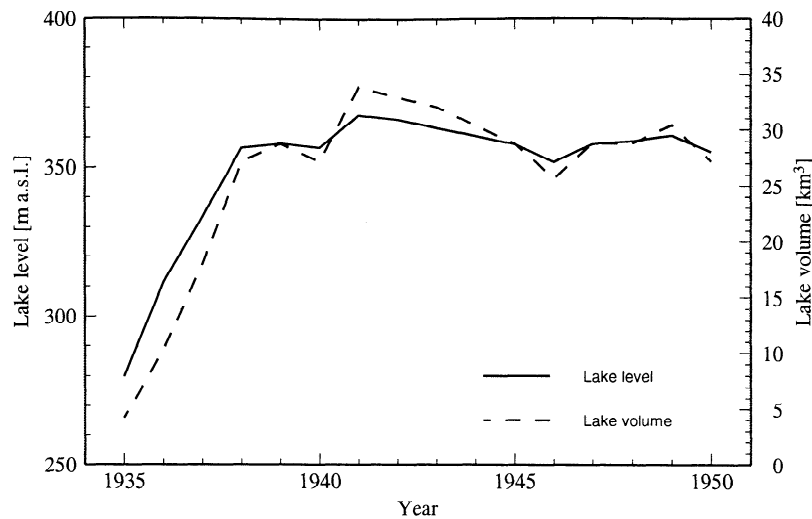
Figure 3. Lake level history of Lake Mead measured at Hoover Dam [*Langbein*, 1960] and corresponding volume derived in this study.

bench mark BM_i is the sum of the height H_0 of the reference bench mark BM_0 and all section heights between BM_0 and BM_i, $H_i = H_0 + \sum_i dh_i$. Releveling of an existing leveling line detects changes in elevation of a particular bench mark. The elevation change Δh_i of bench mark BM_i between times t_1 and t_2 is given as $\Delta h_i = H_i(t_2) - H_i(t_1)$. Leveling surveys are subdivided into first-, second-, and third-order levelings. The first-order leveling is the most precise. Each order is subject to a field tolerance β (in mm). Each section of a line is surveyed both in forward and backward directions, resulting in double-run sections. Each section is resurveyed until the desired field tolerance is met.

Several first-order geodetic levelings were undertaken by the National Geodetic Survey (NGS) in the Lake Mead area after the construction of Hoover Dam to monitor the deformation related to the filling of Lake Mead [*Parkin*, 1960; *Lara and Sanders*, 1970]. The first leveling in March and April 1935 established the basic network. It was run shortly after the lake started to fill and represents the minimum water load condition. In 1935 a network of 1140 km of bench marks (lines 1-11) was leveled. From October 1940 to April 1941 the entire network was leveled. In this and the following surveys, lines crossing the lake were connected by tide gages. In 1941, in addition to lines 1-11 a new line between Chloride and Pattersons Well was added to the net. This line was not revisited afterward and does not enter into our analysis. The 1940-1941 network comprised 1144 km of lines. During the third survey from December 1949 to July 1950 a network of 931 km of lines was leveled (lines 3-5, 7, and 8-11). During the fourth survey from April to June 1963 [*Lara and Sanders*, 1970] a network of 585 km of lines was leveled (lines 3, 4, 5, 6, 10, and 11). In 1983, parts of lines 5, 6, and 9 were leveled. Unfortunately, the spur line from Moapa to Cane Springs was not leveled in 1983, and these elevations cannot be differenced with the 1935 elevations. All levelings were first-order levelings with an accuracy of 3–4 mm $\sqrt{L}$, with L the total line length in km. For simplicity, we refer to the surveys in the following as 1935, 1941, 1950, 1963, and 1983 surveys (see Table 1).

The 1935 and 1941 surveys were carried out between October and April, a time when the lake level is relatively low. The 1950 and 1963 surveys were completed in July and June; thus the lake level at the end of the latter two surveys was 20% higher than at the end of the 1935 and 1941 surveys due to seasonal variations. This difference in lake level corresponds to a difference in the water load of 25% (Figure 3).

In this paper we use the elevation differences published in Table 2.1 of *Lara and Sanders* [1970]. The measurements in 1935, 1941, and 1950 are described by *Parkin* [1960]. The elevation differences are based on the assumption that the elevation of the Cane Springs bench mark remained unchanged. According to *Parkin* [1960], measurements which are part of a circuit are corrected for circuit misclosures. For the 1935 survey the average rate of adjustment corrections was 0.19 mm/km with a maximum of 0.39 mm/km on a 59-km line. For the 1941 survey the average adjustment rate was 0.11 mm/km with a maximum of 0.25 mm/km on a 128-km line. For the 1950 survey the average adjustment rate was 0.14 mm/km with a maximum of 0.29 mm/km on a 29-km line. For the 1963 survey, *Lara and Sanders* [1970] give an average rate of adjustment of 0.35 mm/km, and the maximum rate was 0.85 mm/km. For the 1935 survey, 130 km not part of a circuit (spur lines) were not adjusted. For the 1941 survey, 188 km were excluded from the adjustment. This includes spur lines and the northern part of line 8 (Lake Shore mine gage to 16 km east of St Thomas, Nevada) for which the closures of 0.1 m and opposite sign were nearly twice the allowable limit. Parkin finally fitted this line into the adjusted network with a correction of 1.77 mm/km. The 3 mm $\sqrt{L}$ criterion would allow a rate of 0.41 mm/km for this 54-km line. We use this line only as supplementary information. For the 1950 survey, 62 km of spur lines were excluded from the adjustment. *Lara and Sanders* [1970] do not give a number for the length of lines excluded from the adjustment for the 1963 survey.

Parkin [1960] and *Lara and Sanders* [1970] mention a supplementary adjustment in which the 1935 network was adjusted to sea level datum of 1929 by holding as fixed the

Table 1. Selected Leveling Lines Surveyed During the Various Campaigns

NGS Number	Date	Order/Class	Tolerance β, mm	Deviation α_D, mm	Line Length L, km	Signal-to-Noise SNR	
			Line 5, Las Vegas to Cane Springs, Nevada				
L6315	March 1935 - April 1935	1/2	4.0	1.08	111.12	3.84	(71)
L9095	Dec. 1940 - Feb. 1941	1/2	4.0	1.33	110.83	3.84	(71)
L13431	Dec. 1949 - April 1950	1/1	3.0	1.23	109.96	6.51	(71)
L19225	April 1963 - May 1963	1/2	4.0	1.38	114.66		
L24739	Jan. 1983 - April 1983	1/2	4.0	0.85	227.25		
			Line 8, Pattersons Well, Arizona to St. Thomas, Nevada				
L6310	March 1935 - April 1935	1/2	4.0	1.24	94.28		
L9101/1	Feb. /1941 - March 1941	1/2	4.0	1.37	28.64	4.04	(84)
L9101/2	March 1941 - March 1941	1/2	4.0	1.36	53.13	4.04	(84)
L13512/1	Feb. 1950 - Aug. 1950	1/1	3.0	1.21	24.37	4.60	(80)
L13512/2	April 1950 - Aug. 1950	1/1	3.0	1.30	49.02	4.60	(80)
			Line 9, Boulder City, Nevada to Chloride, Arizona				
L6314	March 1935 - April 1935	1/2	4.0	1.13	94.37		
L9076/1	Sept. 1940 - Feb. 1941	1/1	3.0	1.30	94.51	1.89	(119)
L9076/2	Feb. 1941 - Feb. 1941	1/1	3.0	1.38	5.83	1.89	(119)
L13460	March 1950 - April 1950	1/1	3.0	1.24	94.28	3.25	(117)
L19231	May 1963 - June 1963	1/2	4.0	1.39	92.49	3.25	(117)
			Line 10, Las Vegas to Searchlight, Nevada				
L5993	March 1935 - March 1935	1/2	4.0	1.18	90.38		
L9055	Dec. 1940 - Feb. 1941	1/1	3.0	1.17	94.25	4.12	(58)
L13429	Dec. 1949 - Jan. 1950	1/1	3.0	1.19	92.17	3.91	(49)
L19228	May 1963 - June 1963	1/2	4.0	1.36	91.78		
			Line 11, Las Vegas, Nevada to Chloride, Arizona				
L6312	March 1935 - April 1935	1/2	4.0	1.16	119.65		
L9079/1	Jan. 1941 - Feb. 1941	1/1	3.0	1.26	59.63	1.74	(80)
L9079/2	Jan. 1941 - Feb. 1941	1/1	3.0	1.31	38.32	1.74	(80)
L13514/1	Feb. 1950 - Aug. 1950	1/2	4.0	1.23	60.14	3.95	(80)
L13514/2	June 1950 - Aug. 1950	1/2	4.0	1.28	37.99	3.95	(80)
L19234	April 1963 - July 1963	1/2	4.0	1.35	84.98		

The signal-to-noise ratio is taken for differences in elevation relative to the 1935 reference survey; the numbers in parantheses are bench marks available. All lines are double-run surveys.

elevations resulting from the Cane Springs adjustment for a ring of junctions on the perimeter of the net. The purpose of this supplementary adjustment was to make the elevations consistent with the surrounding control. *Parkin* [1960] was not very clear as to whether the supplementary adjustment was been applied to the published data. Since both *Parkin* [1960] and *Lara and Sanders* [1970] note that the warping due to the fitting to the older data can be problematic for deriving changes in elevation, we are confident that the supplementary adjustment has either been applied to all surveys or to none; thus it has no effect on our analysis.

Our analysis is based on a subset of the leveling data (see Table 1) to reduce the amount of computation time. A total of 818 bench marks is used that are taken from lines 5, 8, 9, 10, and 11 and the 1935, 1941, and 1950 leveling campaigns.

3.3. Leveling Errors

Leveling data may be contaminated by systematic and random errors. Systematic errors ϵ_s arise, for example, from miscalibrated rods or from atmospheric refraction and can accumulate along the leveling line. Systematic errors often result in a correlation between observed tilt difference and bench mark elevation. We plotted the tilt differences against elevations for all lines, and we did not find systematic trends.

This indicates that the leveling data used in this study are not grossly contaminated by systematic errors.

Random errors arise from a variety of processes, such as inaccurate instrument readings or incorrectly noted data (blunders). As random errors accumulate along a line with the square root of total line length, the standard deviation α_D (mm) of a double-run line can be used to derive the allowable random error, $\epsilon_r = \alpha_D \sqrt{L}$ (mm), with the total line length L (km) [*Marshall et al.*, 1991].

Here α_D can be derived from several methods, such as differences between forward and backward runs and loop misclosures. In the first case, we find

$$\alpha_D = \frac{1}{N} \sum_{i=1}^{N} \sqrt{\frac{V}{L_i}}, \tag{1}$$

with N the number of double-run sections per line, n the number of reruns for each section, V the variance, with $V = 1/n \sum_i (dh_i - dh_{ave})^2$, where dh_{ave} is the average section height, $dh_{ave} = 1/n \sum_i dh_i$, and L_i the ith section length (km) [e.g., *Murray et al.*, 1996]. In the second case the misclosure ϵ_{mis} (mm) is used to derive the standard deviation from $\alpha_D = \epsilon_{mis}/\sqrt{L_i}$. For NGS surveys, α_D is listed with the leveling data.

For two different levelings taken at times t_1 and t_2 the uncertainty in elevation change is given as

$$\delta^2 = \alpha_D(t_1)^2 + \alpha_D(t_2)^2. \qquad (2)$$

The uncertainty in elevation change between two adjacent bench marks is given by

$$\sigma_i = \sqrt{\delta^2 L_i + \Delta\delta^2}, \qquad (3)$$

with $\Delta\delta$ an additional uncertainty to account for unmodeled adjustments along faults and for local subsidence. We assume $\Delta\delta = 2$ mm. Although larger values of $\Delta\delta$ improve the fit of the leveling data, the best fitting solution is independent of the absolute value. While δ is constant for the entire line, σ_i varies for every bench mark. In this study, σ_i is between 3 and 5 mm. To measure the relevance of the surveyed elevation change relative to the uncertainties in elevation change, we define a signal-to-noise (SNR) ratio for each line [e.g., *Marshall et al.*, 1991],

$$\text{SNR} = \sqrt{\frac{1}{n}\sum_{i=1}^{n}\left(\frac{\Delta h_i}{\sigma_i}\right)^2}. \qquad (4)$$

A SNR of 1 means the average elevation change of the order of the uncertainties, and a larger value indicates better resolving power for the rheological structure. We observe a generally better signal-to-noise ratio for the 1950 leveling campaign (Table 1), which is due to the larger subsidence at that time.

Figure 4 shows an example of the leveling data for lines 9 and 11. The surveys of 1941 and 1950 detect a large-scale and progressive subsidence relative to 1935, which is largest in the middle of the line in the Virgin Basin area for line 11. The deformation is clearly associated with the water load of Lake Mead, and the maximum subsidence is 122 mm in 1941 and 217 mm in 1950. The 1963 survey indicates rebound, as the maximum subsidence of 200 mm is smaller than in 1950. However, since the area is heavily faulted (Figure 2), the measured deformation is likely to be influenced by movement along faults, especially on line 8.

After the filling of Lake Mead, seismicity increased significantly [*Carder and Small*, 1948; *Longwell*, 1960a; *Rogers and Lee*, 1976]. Most of the events are shallower than 13 km. An event with magnitude 5 occurred shortly before the 1963 leveling [*Lara and Sanders*, 1970; *Rogers and Lee*, 1976]. The uplift in the Boulder and Virgin Basins detected in the 1963 survey can possibly be attributed to this event.

Lara and Sanders [1970] concluded that the subsidence in the Lake Mead area ceased around 1950. This corresponds to a relaxation time of $t \sim 25$ years. Using the relation
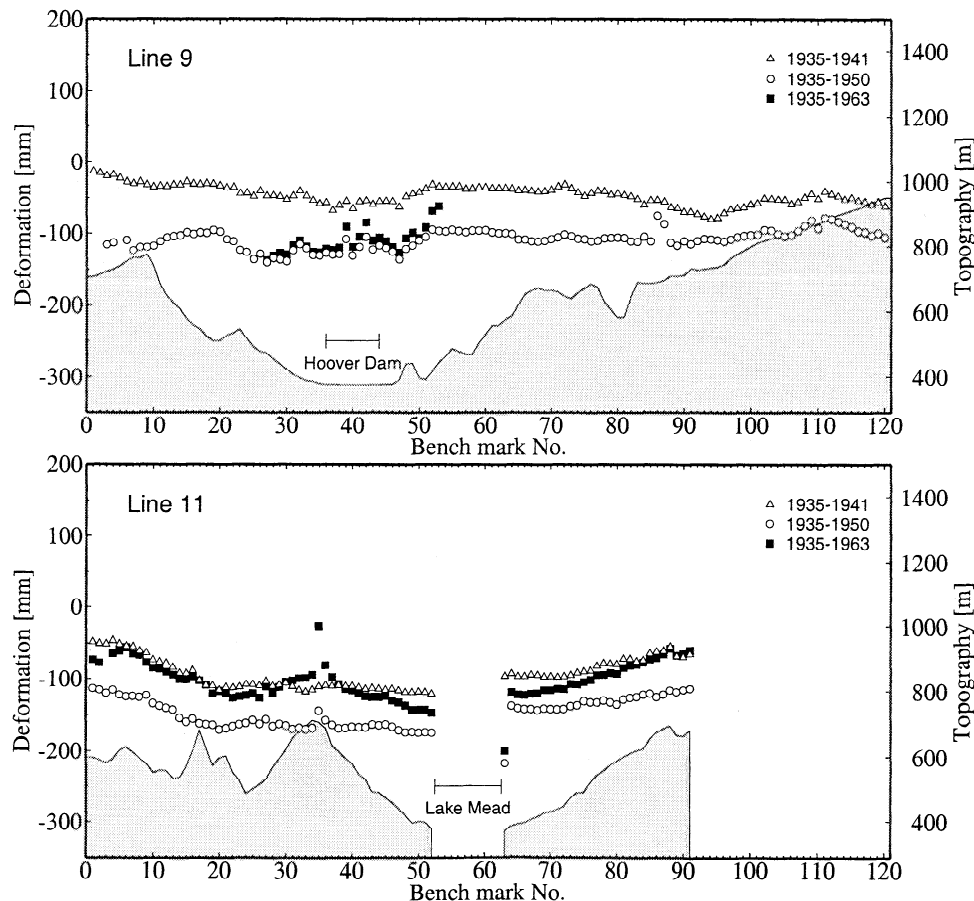

Figure 4. Vertical surface deformation along lines (top) 9 and (bottom) 11 relative to the 1935 survey from levelings in 1941, 1950, and 1963. Note that line 11 is discontinuous across the lake, and the shaded area represents the topography along the line.

for the Maxwell relaxation time $t = \eta/\mu$, [e.g., *Turcotte and Schubert*, 1982] and the average shear modulus $\mu \simeq 10^{10}$ Pa, the viscosity η of the subcrust must be of the order of $10^{18} - 10^{19}$ Pa s.

4. Theory

4.1. Formulation of the Problem

We calculate surface deformations associated to changes in the water load for different Earth models. We consider a flat, compressible, Maxwell-viscoelastic continuum consisting of $K - 1$ layers ($k = 1, K - 1$) of thickness h_k, overlying an infinite half-space ($h_K \to \infty$). The density ρ_k, shear modulus μ_k, bulk modulus K_k, and viscosity η_k are homogeneous within each layer but can vary between layers. This modeling approach is similar to other load-induced deformation studies [e.g., *Ward*, 1985; *Wolf*, 1985a; *Bills et al.*, 1994]. However, for comparison with observed leveling data we also account for the warping of the geoid as a result of both internal and external mass redistributions [see *Solling*, 1950; *Wolf*, 1985b] to obtain surface deformations relative to the geoidal surface.

We solve the equation of motion, the Maxwell-viscoelastic constitutive equation, and the Poisson equation by transforming the time-dependent field quantities into the Laplace-transformed domain. Thus the Laplace-transformed viscoelastic equations are similar to the equivalent set of elastic equations, as stated by the correspondence principle [e.g., *Biot*, 1962; *Peltier*, 1974]. The Laplace-transformed equations then read

$$\begin{aligned}
\tilde{t}_{ij,j} &= -(\rho g_j \tilde{u}_j)_{,i}, \\
\tilde{t}_{ij} &= \tilde{\lambda}\tilde{u}_{k,k}\delta_{ij} + \tilde{\mu}(\tilde{u}_{i,j} + \tilde{u}_{j,i}), \quad (5) \\
\tilde{\phi}_{,ii} &= 0.
\end{aligned}$$

Here the tilde denotes a Laplace-transformed field quantity, t_{ij} is the Cauchy stress tensor, u_i is the displacement vector, ϕ is the gravitational potential, g_i is the gravitational acceleration, and δ_{ij} is the Kronecker delta. The indices range between 1 and 3, and repeated indices within a term imply summation over this index. In equation (5) we implicitly assume that (1) the continuum is isotropic and isochemical, (2) the bulk modulus is elastically compressible, $K(t) = K$ and $\lambda(t) = K - \frac{2}{3}\mu(t)$, (3) the shear modulus is time-dependent according to $\mu(t) = \mu_0 \exp(-\alpha t)$, $\alpha = \mu_0/\eta$, and μ_0 the seismically inferred shear modulus, and (4) the gravitational field is homogeneous. The latter assumption decouples the mechanical and gravitational field equations.

We solve (5) subject to a set of boundary conditions. Within the continuum, u_i, t_{ij}, ϕ, and $\phi_{,i} - 4\pi G\rho u_i$ are continuous across each interface. At the surface a load q is applied in the direction normal to the surface,

$$\begin{aligned}
[\tilde{u}_i] &= 0, \\
[n_j\tilde{t}_{ij}] &= -\tilde{q}, \\
[\tilde{\phi}] &= 0, \quad (6) \\
\left[n_i(\tilde{\phi}_{,i} - 4\pi G\rho\tilde{u}_i)\right] &= -\frac{4\pi G}{g_i}\tilde{q}.
\end{aligned}$$

Here G is Newton's gravitational constant, and n_i is the unit normal at the surface. We introduce a cylindrical coordinate system (r, z), assuming axial symmetry and define z as depth positive downwards into the continuum. Thus $g_i = (0, 0, g)^T$. The load q is given as $q(r, t) = q_1(r)q_2(t)$, with the load geometry $q_1(r) = \rho_w g h_w$ for $r \leq r_w$; ρ_w, r_w, and h_w are the load density, radius, and height, respectively. The time dependence is assumed to be impulsive, $q_2(t) = \delta(t)$, and a more realistic loading history can be derived by convolution. We then apply a Hankel transformation of zeroth order to u_z, t_{zz}, and q and of first order to u_r and t_{rz}. Hankel-transformed field quantities are identified by capitals.

The mechanical field equations are then recast into the matrix equation

$$\frac{\partial \tilde{F}(k, z, s)}{\partial z} = \tilde{M}(k, z, s)\tilde{F}(k, z, s), \quad (7)$$

with k the wave number, s the Laplace frequency, $\tilde{F} = [\tilde{U}_r, \tilde{U}_z, \tilde{T}_{rz}, \tilde{T}_{zz}]^T$, and $\tilde{M}$ the rheology matrix for the kth layer as given in (A1).

For two starting solutions at the top of the half-space at $z = z_K$ such as

$$\begin{aligned}
\tilde{F}^1(k, z_K, s) &= [1, 1, -2\tilde{\mu}k, -(2\tilde{\mu}k + \rho g)]^T e^{-kz_K}, \\
\tilde{F}^2(k, z_K, s) &= [1, -\frac{\tilde{\mu}}{\lambda + 2\tilde{\mu}}, -2\tilde{\mu}k\left(\frac{\lambda + \tilde{\mu}}{\lambda + 2\tilde{\mu}}\right), \\
&\quad \rho g\frac{\tilde{\mu}}{\lambda + 2\tilde{\mu}}]^T e^{-kz_K}, \quad (8)
\end{aligned}$$

we can propagate the starting solution (8) to the surface $z = z_0$, using

$$\begin{aligned}
\tilde{F}^1(k, z_0, s) &= \tilde{P}(k, z_K, z_0, s)\tilde{F}^1(k, z_K, s), \\
\tilde{F}^2(k, z_0, s) &= \tilde{P}(k, z_K, z_0, s)\tilde{F}^2(k, z_K, s), \quad (9)
\end{aligned}$$

with $\tilde{P}(k, z_K, z_0, s)$ the product of all layer propagators as listed in (A2),

$$\tilde{P}(k, z_K, z_0, s) = \prod_{k=1}^{K-1} \tilde{P}_k(k, z_k, z_{k-1}, s). \quad (10)$$

Finally, we apply the two remaining boundary conditions (6) at $z = z_0$,

$$\begin{aligned}
a\tilde{T}_{rz}^1(k, z_0, s) + b\tilde{T}_{rz}^2(k, z_0, s) &= 0, \\
a\tilde{T}_{zz}^1(k, z_0, s) + b\tilde{T}_{zz}^2(k, z_0, s) &= -\tilde{Q}(k, s), \quad (11)
\end{aligned}$$

with $\tilde{Q}$ the Hankel-transformed surface load. By solving (11) for a and b we have determined the surface deformation field,

$$\tilde{F}(k, z_0, s) = a\tilde{F}^1(k, z_0, s) + b\tilde{F}^2(k, z_0, s), \quad (12)$$

which then is transformed back by an inverse Laplace and an inverse Hankel transformation into the temporal and spatial domain.

For the inverse Laplace transformation we partition the solution vector $\tilde{F}$ into an elastic and a viscous part:

$$\tilde{F}(k, z_0, s) = F^e(k, z_0) + \tilde{F}^v(k, z_0, s). \quad (13)$$

The elastic part is readily derived from

$$F^e(k, z_0) = \lim_{s \to \infty} \bar{F}(k, z_0, s). \qquad (14)$$

For the viscous part we assign a set of collocation points in the Laplace-transformed domain, $s = s_i$, which sample the relaxation times $1/s_i$ evenly over the entire time interval of interest [e.g., *Schapery*, 1961; *Mitrovica and Peltier*, 1992]. We then can solve the set of equations

$$\tilde{F}^v(k, z_0, s_i) = \sum_j \frac{b_j(k, z_0)}{s_i + s_j}, \qquad (15)$$

for the vector $b_i(k, z_0)$. We calculate the time domain response of the viscous part as

$$F^v(k, z_0, t) = \sum_i b_i(k, z_0)e^{-s_i t}, \qquad (16)$$

with t the time, and reassemble the time-dependent solution vector as

$$F(k, z_0, t) = F^e(k, z_0) + F^v(k, z_0, t). \qquad (17)$$

A similar procedure is used to solve Poisson's equation in the Laplace and Hankel-transformed domain [e.g., *Breuer and Wolf*, 1995]. After inverse Laplace transformation we arrive at

$$\Phi(k, z_0, t) = -\frac{2\pi G}{k} \left[\frac{Q(k, t)}{g} - \sum_{k=1}^{K} (\rho_k - \rho_{k-1}) \right.$$
$$\left. \times \quad U_z(k, z_k, t)e^{-k(z_k - z_0)} \right]. \qquad (18)$$

From (18) we apply Bruns' formula [*Heiskanen and Moritz*, 1967] and obtain the geoid height deformation as

$$E_z(k, z_0, t) = \frac{\Phi(k, z_0, t)}{g}. \qquad (19)$$

Finally, we apply an inverse Hankel transformation and derive our predicted surface deformation between two levelings carried out at times t_1 and t_2 for the ith bench mark,

$$p_i = [u_z(r, z_0, t_2) + e_z(r, z_0, t_2)]$$
$$-[u_z(r, z_0, t_1) + e_z(r, z_0, t_1)]. \qquad (20)$$

In (20), $p_i = p_i(a_j)$ is a function of the rheology of the proposed Earth model, indicated by the parameter vector a_j.

4.2. Forward Problem

We adopt two strategies to infer the Earth models, which best fit the observed leveling data. The first strategy is a forward modeling procedure with simple two- and three-layer Earth models. The quantities of interest for layer k are the thickness h_k and the viscosity η_k. For each set of Earth models, two of the h_k and η_k are free, and the remaining are fixed to some value. The two-dimensional parameter space is then systematically explored with forward calculations by

varying the free parameters within a given interval and calculating a χ^2 merit function between observed and predicted deformation for a given pair of parameters:

$$\chi^2(a_k) = [o_i - p_i(a_k)] \, [Co_{ij}^d]^{-1} \, [o_j - p_j(a_k)]. \qquad (21)$$

Here, the $o_i, i = 1, n$ are the observed elevation changes at the ith bench mark relative to the Cane Springs bench mark and $p_i(a_j)$ are the model predictions. The Earth model parameter vector a_i represents the two free model parameters, e.g., the thickness of the elastic crust and the viscosity of the subcrust. We define the data covariance matrix Co_{ij}^d [*Arnadottir et al.*, 1992] as

$$Co_{ij}^d = \delta^2 \left\{ \begin{array}{ll} SL_j, & j \leq i \\ SL_i, & j > i \end{array} \right\} i, j = 1, n, \qquad (22)$$

with SL_i the total distance from the first bench mark in each line to the actual ith bench mark and δ given by (2). If the leveling data are uncorrelated, the data covariance matrix simplifies to $Co_{ij}^d = \sigma_i^2 \delta_{ij}$.

From (21) we derive the root-mean-square (rms) value as

$$\epsilon(a_k) = \sqrt{\frac{1}{n}\chi^2(a_k)}, \qquad (23)$$

in the following referred to as misfit function. The rms value identifies the Earth model a_k, which best satisfies the leveling data within the observational uncertainties and the adopted model parameter space. If the model parameter space is complete and the observational uncertainties are normally distributed with known standard deviations, the expected rms is 1. However, we do not expect to fit the leveling data to this accuracy because our continuum model does not account for discontinuous movements along faults. Thus it is likely that ϵ will exceed 1.

The rms value does not, however, indicate the range of Earth models, which also satisfy the observations within their uncertainties. We therefore introduce the statistic γ [*Lambeck et al.*, 1998] as

$$\gamma^2(a_k) = \frac{1}{n} [\hat{p}_i - p_i(a_k)] \, [Co_{ij}^d]^{-1} \, [\hat{p}_j - p_j(a_k)], \qquad (24)$$

with $\hat{p}_i$ the model prediction, which results in the minimum value for χ^2. The statistic γ^2 has a χ^2 distribution with $n - 4$ degrees of freedom, and model predictions with $n\gamma^2 \leq \chi^2|_{n-4,\zeta}$ satisfy the leveling data at the ζ confidence limit.

4.3. Inverse Problem

Our second strategy is used to infer more complicated radial variations in Earth model properties. Here, the forward modeling approach quickly becomes inefficient, and a formal inverse procedure to minimize the difference between predictions and observed leveling data is more appropriate. The nonlinear inverse problem is given as

$$o_i = p_i(a_j), \quad i = 1, n, \quad j = 1, m, \qquad (25)$$

with $a_i, i = 1, m$ the Earth model parameter vector, and m

the number of free parameters. We find a_i by minimizing the sum of χ^2 and D, $\min\{\chi^2 + D\}$, with χ^2 given by (21) and D the weighted length of the model parameter space [e.g., *Menke*, 1989],

$$D = [a_i - a_i^0] \, [Co_{ij}^m]^{-1} \, [a_j - a_j^0].\qquad(26)$$

Here, Co_{ij}^m is the model covariance matrix, containing information about the uncertainty of the model parameter space Δa_i on the main diagonal and possible dependencies between model parameters as off-diagonal elements,

$$Co_{ij}^m = 2\Delta a_i^2 \left\{ \begin{array}{ll} 1, & i=j \\ \exp[-\frac{\Delta h^2}{2c^2}], & i \neq j \end{array} \right\} i,j = 1, m, \quad(27)$$

with $\Delta h = h_i - h_j$ the distance between the ith and the jth layer and c the correlation length. For $c = 0$ the model covariance matrix has completely independent model parameters. However, we use $c = 10$ km to enforce a smoothness constraint on the viscosity profile over this length. For the model parameter uncertainty we have chosen $\Delta a_i = 0.03$ to stabilize the solution. We use the best fitting model from the forward procedure as a priori value a_i^0 of a_i.

Following *Tarantola and Valette* [1982], we minimize $\chi^2 + D$ by differentiating with respect to a_i and setting it to zero. As our model is nonlinear in p_i, we apply an iterative approach to infer the best fitting a_i. This implies calculating the Frechet kernel matrix $J_{ij} = \partial p_i / \partial a_j$. For a given a priori model parameter vector a_i^0 we then can improve the solution iteratively for the $(k + 1)$th step as

$$\begin{aligned} \mathbf{a_{k+1}} = \;& \mathbf{a_0} + \left\{ \mathbf{J_k}^T [\mathbf{Co^d}]^{-1} \mathbf{J_k} + [\mathbf{Co^m}]^{-1} \right\}^{-1} \\ & \times \mathbf{J_k}^T [\mathbf{Co^d}]^{-1} [\mathbf{o} - \mathbf{p_k} + \mathbf{J_k}(\mathbf{a_k} - \mathbf{a_0})]. \end{aligned} \quad(28)$$

Here, bold field quantities are used as short-term notations for vector and matrix fields. The a posteriori model covariance matrix can be used to assess the reliability of the inverse solution. It reads

$$\mathbf{Co}_{\text{post},k}^m = \left\{ \mathbf{J_k}^T [\mathbf{Co^d}]^{-1} \mathbf{J_k} + [\mathbf{Co^m}]^{-1} \right\}^{-1}. \quad(29)$$

Note that (29) is only meaningful if model predictions are weakly nonlinear with respect to a_i [e.g., *Snieder*, 1998]. This is achieved by solving for the logarithm of the viscosity in 10 layers of predescribed thickness.

5. Results

In this section we infer an Earth model, which satisfactorily explains the leveling data and which is as simple as possible. We compare the observed subsidence with numerical predictions for a set of different Earth models to infer the rheological structure of the Earth's crust and subcrust. Models with a minimum discrepancy between observed and predicted deformation are considered representative for the Earth's rheological structure. The elastic structure (density, shear, and bulk modulus) is taken from *Priestley et al.* [1980] and is based on surface waves and seismic refraction data. Here a 35-km-thick crust is underlain by a high-velocity layer of 29 km thickness and a low-velocity zone of 120 km thickness. For our best fitting models the minimum misfit of (23) is $\epsilon \simeq 10 - 15$, indicating that we cannot predict the observed subsidence within the uncertainties of the data. As stated earlier, we do not expect our predictions to fit the observations to that degree, as our viscoelastic continuum model cannot simulate the discontinuous movement along faults, which is observed in the leveling data.

In the forward procedure the two-dimensional parameter space is systematically explored with forward calculations by varying the two free parameters within a given interval and calculating a misfit between observed and predicted deformation for a given pair of parameters. The inverse procedure allows the inference of a more complex rheological structure, as we subdivide the Earth model into 10 layers and treat the layer viscosities as free parameters. The viscosity in each layer is correlated to neighboring values, as the correlation length in (27) is fixed to 10 km. This correlation length damps the deviation of viscosity between layers in order to infer relatively smooth variations of viscosity with depth.

5.1. Thickness of the Crust and Viscosity of the Subcrust

We first use the leveling data of lines 5, 9, 10, and 11 of the 1941 and 1950 surveys to constrain the thickness of the elastic crust and the viscosity of the subcrust, based on a two-layer Earth model M2 (Table 2). We have omitted line 8 at this stage, as the data indicate strong discontinuous movement along faults, and the adjustment correction applied by *Parkin* [1960] is 4 times larger than the allowable limit. We first employ the forward modeling strategy and assume that the data are uncorrelated, $Co_{ij}^d = \sigma_i^2 \delta_{ij}$. The two free Earth

Table 2. Parameters of Two-Layer Earth Model

Model	Layer	Viscosity η, Pa s	Thickness h, km
M2	crust	∞	$h_1 \in [10, 70]$
	subcrust	$\eta_2 \in [3.16 \times 10^{17}, 10^{20}]$	∞

Earth model is calculated every 10 km for h_1, and two per decade for η_2, resulting in 42 models.
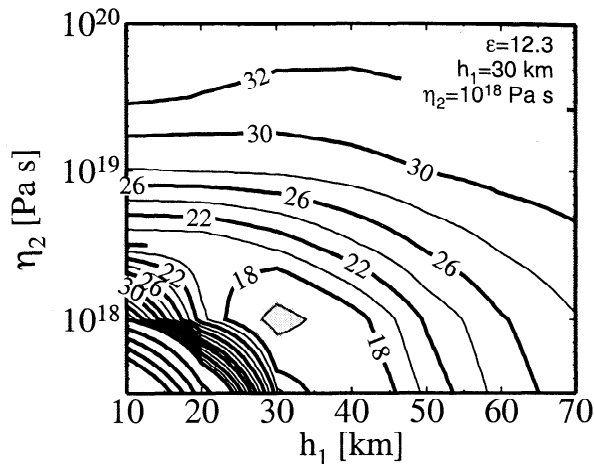
Figure 5. Misfit between observed and modeled deformation for two-layer Earth model M2 as a function of crustal thickness h_1 and subcrustal viscosity η_2. The data used are lines 5, 9, 10, and 11 from the 1941 and 1950 surveys and are assumed to be uncorrelated. The shaded region indicates the 99% confidence limit. The numbers in the legend are the misfit value ϵ and the free parameters for the best fitting model.

model parameters are the crustal thickness h_1 and the subcrustal viscosity η_2. The results are presented in form of a two-dimensional misfit function, and the best fitting parameters for a set of Earth models are given by the minimum misfit. The interval for the free parameters is chosen to ensure that the minimum misfit represents a global minimum.

The misfit function (Figure 5) has a clear minimum for $h_1 \simeq 30$ km and $\eta_2 \simeq 10^{18}$ Pa s. These values represent the

crustal thickness and subcrustal viscosity of the two-layer Earth model that best fits the observations. Misfit values increase rapidly further away from the global minimum, an indication that both free Earth model parameters are well constrained by our continuum model approach. However, the minimum misfit of $\epsilon = 12.3$ indicates that the majority of the predictions cannot fit the observations within the observed uncertainties. As we discuss in section 5.3, the apparent contradiction between well-constrained Earth model parameters and the poor fit of model predictions to leveling data at individual bench marks is a result of local deformations not directly associated with the Lake Mead water load.

We have derived the set of Earth models, which satisfy the leveling data within their uncertainties to the 99% confidence limit by predicting the statistic (24). Thus values smaller than 1 indicate that two predictions p_i and $\hat{p}_i$ can fit the observed data equally well within the uncertainties of elevation change given. The shaded area in Figure 5 identifies the confidence limit, which is fairly small and suggests uncertainties of ± 3 km for h_1 and ± 0.2 for $\log \eta_2$.

In Figure 6 we test the reliability of this result using the same two-layer Earth model but different subsets of the leveling data. The subsets are lines 5, 9, 10, and 11 of the 1941 leveling data (Figure 6a), lines 5, 9, 10, and 11 of the 1950 leveling data (Figure 6b), and lines 8, 9, 10, and 11 (Figure 6c), and lines 9, 10, and 11 (Figure 6d) of the 1941 and 1950 leveling data. For all data subsets the minimum misfit is found for $h_1 = 30$ km and $\eta_2 = 10^{18}$ Pa s. With the 1941 leveling data alone a smaller misfit ($\epsilon = 9$, Figure 6a) is achieved than with the entire data set ($\epsilon = 12$, Figure 5). However, the model parameters are less well constrained, as
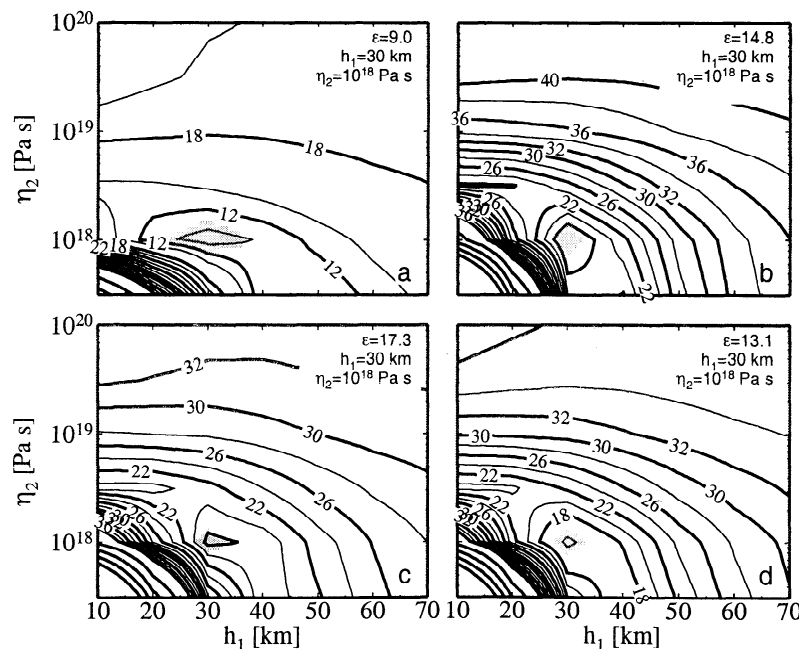

Figure 6. Misfit between observed and modeled deformation for two-layer Earth model M2 as a function of crustal thickness h_1 and subcrustal viscosity η_2 for different subsets of the leveling data. (a) Lines 5, 9, 10, and 11 of the 1941 survey, (b) lines 5, 9, 10, and 11 of the 1950 survey, (c) lines 8, 9, 10, and 11 of the 1941 and 1950 surveys, and (d) lines 9, 10, and 11 of the 1941 and 1950 surveys.

indicated by a small relief of the misfit function. This is related to the small amount of deformation which occurred until 1941. The minimum misfits for the 1950 data alone ($\epsilon = 14.8$, Figure 6b) and using the same data as for Figure 5 but replacing line 5 with line 8 ($\epsilon = 17.3$, Figure 6c) are higher than in Figure 5, but the minima are well defined in both cases. The higher misfit values are clearly associated to the larger proportion of lines having less smooth elevation changes. Using the same data as for Figure 5 but omitting line 5 to sample the vicinity of the two major basins, we also obtain a similar misfit pattern ($\epsilon = 13.1$, Figure 6d). Thus the parameters of the best fitting model are robust against different subsets of the leveling data.

We then tested the influence of the correlation among the leveling data, the influence of the value of the uncertainties in elevation change, and the influence of outliers in the leveling data on our result. Taking into account the full covariance matrix (22), we obtained essentially the same best fitting model. This indicates that the correlations among the leveling data represented by the off-diagonal elements of (22) are not important and for computational efficiency can be neglected. In order to obtain a misfit value of 1, we need to multiply the uncertainties in elevation change σ_i (3) by a factor of 20. However, the increased σ_i do not affect the result for the best fitting model. We investigated offsets of 10 mm and 20 mm in the 1950 data and obtained the same best fitting Earth model. For larger offsets the result should be the same, as the pattern of the misfit function does not depend on the off-diagonal elements of (22). Also, reducing the weight of leveling data, which are obviously influenced by local deformation and do not fit to generally smooth lines (e.g., points at bench mark 47 in line 10), by increasing σ_i for that bench mark did not change the results. All this indicates that the crustal thickness of 30 km and the subcrustal viscosity of 10^{18} Pa s are very well constrained by the leveling data.

5.2. Viscosity Profile of the Subcrust

In this section we employ the inverse modeling strategy to explore whether the leveling data provide information about the variation of viscosity with depth. We use the viscosity variation inferred in section 5.1 as the a priori model parameter vector. As this viscosity profile represents the minimum within the two-dimensional parameter space, we expect the inversion to modify the viscosity profile only slightly. From this starting solution we iteratively improve the model parameter vector, using (28), until the weighted least squares solution (21) does not improve significantly. This is typically achieved within three to six iterations.

The resulting viscosity profile is shown in Figure 7. The minimum misfit decreases only from $\epsilon = 12.3$ to 12.0, and the final viscosity profile obtained is similar to the best fitting parameters from section 5.1. The inverse solution indicates that the data do not require a viscosity decrease in the lower part of the crustal layer. This is also indicated by the reductions in uncertainties of the model parameter space Δa_i, which are presented as ratio between pos-

terior ($\Delta \log \eta_{po}$) and prior ($\Delta \log \eta_{pr}$) model uncertainty, $\Delta \log \eta_{po} / \Delta \log \eta_{pr}$. This ratio provides a measure of the resolving power of the leveling data with depth. For $\Delta \log \eta_{po} / \Delta \log \eta_{pr} = 1$, the inversion cannot improve the a priori viscosity profile, while $\Delta \log \eta_{po} / \Delta \log \eta_{pr} < 1$ indicates that the leveling data contain more information for the viscosity in that depth. A significant reduction of the model uncertainty ratio is only achieved below a depth of 30 km. Within the top 30 km the formal inversion cannot improve the a priori viscosity model, except by a slight increase of viscosity between 20 and 30 km depth. As we discuss in section 6.1, this lack of sensibility of the Lake Mead leveling data for the viscosity in the lower crustal region is important to reconcile our results with the lower ductile crust preferred by postseismic deformation studies.

5.3. Best Fitting Earth Model

We now compare the observed and modeled deformation along the five survey lines for the two levelings in 1941 and 1950 (Figure 8). We use the best fitting two-layer model ($h_1 = 30$ km, $\eta_2 = 10^{18}$ Pa s). The model predictions based on the viscosity profile inferred by formal inversion are very similar.

The modeled deformation is far from matching the observations over the entire lines. The fit for lines 5 and 11, and for some parts of lines 8 and 9, is reasonably good. For line 11 the fit could apparently be improved by increasing the warping of the modeled displacement profile using an Earth model with a smaller thickness of the elastic crust. However,
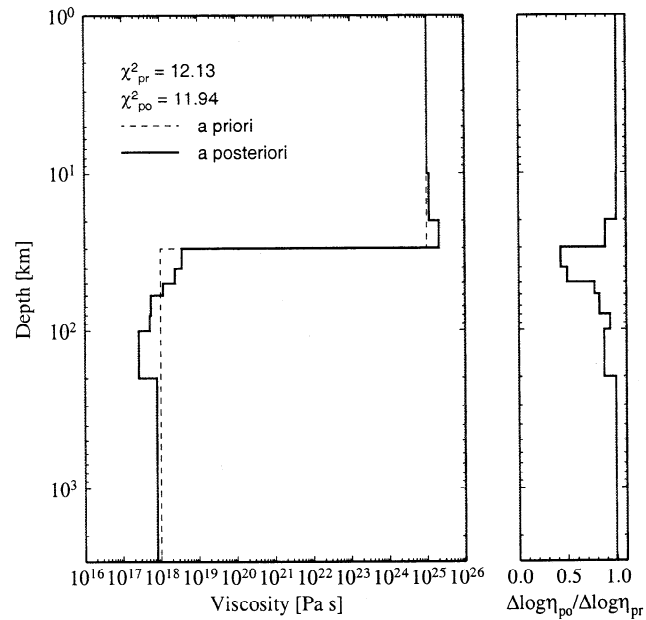

Figure 7. (left) Viscosity profile and (right) ratio of posteriori to priori viscosity uncertainty resulting from the formal inverse procedure. The dashed line is the a priori model as inferred from two-layer forward modeling, and the solid lines are the improved viscosity profile and the viscosity uncertainty ratio. χ^2_{pr} and χ^2_{po} are the a priori and a posteriori least squares misfit, respectively.
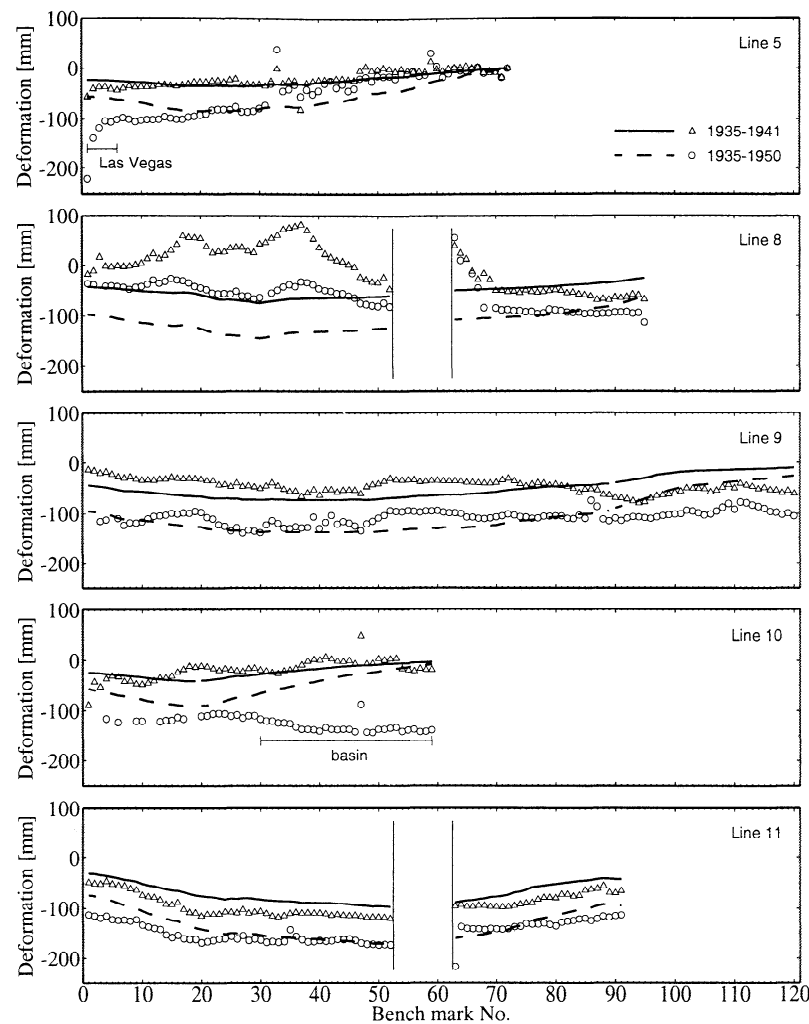
Figure 8. Observed (symbols) and predicted (lines) displacements along four survey lines. The Earth model is the two-layer model M2 with $h_1 = 30$ km and $\eta_2 = 10^{18}$ Pa s. The vertical bars indicate the discontinuity of a line traversing the lake.

this is not possible because a thinner elastic crust would increase the 1950 prediction and the fit would become poorer for all lines. The largest discrepancies occur over the left branch of line 8 and the 1950 data of line 10 as well as the leftmost part of line 5. Here, both observations of line 10 (bench marks 25-59) and line 5 (bench marks 1-10) indicate a local deformation not directly associated with the filling of Lake Mead. Bench marks 1-10 in line 5 are mapping the local groundwater withdrawal from the artesian basin in Las Vegas [*Longwell,* 1960a; *Amelung et al.,* 1999]. Along bench marks 25-59 in line 10, *Longwell* [1960a] noted that the large deformation here can be related to local subsidence of a basin west of Searchlight.

Part of the remaining misfit can also be explained. As already pointed out by *Longwell* [1960a], the subsidence cannot entirely be attributed to the weight of the water load itself. Some basin floors are graben structures, and readjustment along faults may occur here. The induced seismicity has been described by *Carder and Small* [1948] and *Rogers and Lee* [1976]. Load-induced seismicity was detected espe-

cially around the larger basins such as Boulder Basin, suggesting that pre-Pleistocene faults were activated.

In addition, sedimentation occurred since the filling of the lake. In 1948, ~1.75 km^3 of sediment had accumulated in Lake Mead [*Gould,* 1960], reducing the filling capacity of the reservoir by 5%. Most of the sediment was deposited in the Lower Granite Gorge (38%), Boulder Basin (21%), and Virgin and Pierce Basins (both 10%). Only 2.7% had been accumulated in the St. Thomas Overton Arm. Since the sediment volume is small compared to the total reservoir capacity and the density of the water-saturated sediments is relatively low, the effect of sediment loading on the deformation process is negligible.

The predicted subsidence in 1950 for the best fitting two-layer Earth model ($h_1 = 30$ km, $\eta_2 = 10^{18}$ Pa s) is shown as map view in Figure 9. The prediction well reproduces the observed pattern (Figure 1) in the central area. Farther away, the model prediction overestimates the observed subsidence, predicting a generally broader subsidence area. However, as *Longwell* [1960a] noted, the low survey line density around
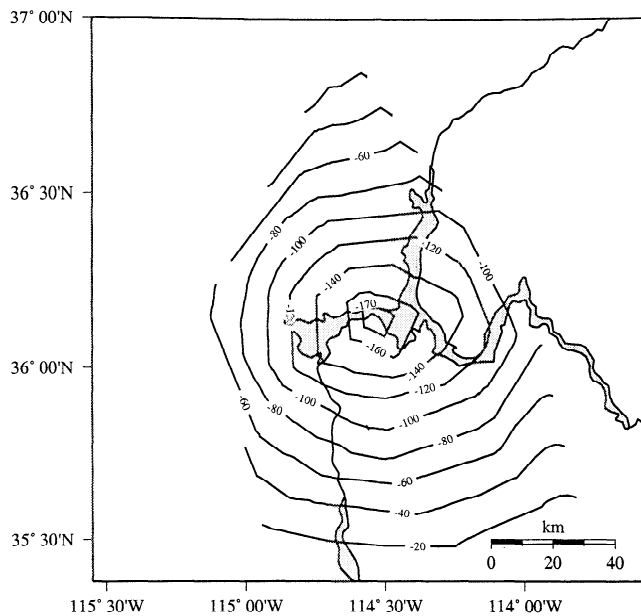
Figure 9. Predicted deformation for 1950 (in mm) for a two-layer Earth model with $h_1 = 30$ km and $\eta_2 = 10^{18}$ Pa s.

Moapa and Searchlight does not provide reliable information on the subsidence pattern in that areas.

6. Discussion

Several authors have inferred the rheological structure of the Earth's crust and subcrust in the Basin and Range Province, using a variety of observations. We now discuss our results deduced from the observations of subsidence from the filling of Lake Mead in view of some of these results. We also compare our results to rheological models based on postglacial rebound and postseismic deformation data.

6.1. Basin and Range Province

The displacement of shorelines of late Pleistocene Lake Bonneville is an important data set for estimating crustal thickness and subcrustal viscosity. The Lake Bonneville region is located 400 km north of Lake Mead and is also in the Basin and Range Province. At the last glacial maximum,

Lake Bonneville encompassed an area of 51,300 km² [*Bills et al.*, 1994]. The surface area of the water load was around 80 times larger than that of Lake Mead.

The results of *Nakiboglu and Lambeck* [1982, 1983] and *Bills and May* [1987] are based on model predictions using Earth models comprising an elastic crust and a viscoelastic subcrust. Estimates of crustal thickness range between 25 and 30 km, consistent with the Lake Mead data. Estimates of subcrustal viscosity are higher than for Lake Mead with values between 2.5×10^{19} and 10^{20} Pa s. *Bills et al.* [1994] analyzed a larger set of shoreline data using layered, viscoelastic Earth models to infer a fairly thin quasi-elastic crust of 10 km thickness. On the basis of a formal inverse procedure, *Bills et al.* [1994] suggest viscosities rapidly decreasing from 2×10^{24} Pa s in the quasi-elastic crust (0-10 km) to values of 10^{21} Pa s in 10-40 km depth, around 10^{18} Pa s between 40 and 80 km depth, and then again increasing to 2×10^{20} Pa s in 150-300 km depth.

The Lake Mead data indicate similarly low viscosities in 30-80 km depth. However, our 30-km elastic crust is significantly thicker than the 10-km crust from *Bills et al.* [1994]. In order to reconcile the different results we introduce a three-layer Earth model M3a (Table 3) with an elastic upper crust of thickness $h_1 = 10$ km, a viscoelastic lower crust of thickness $h_2 = 20$ km with free viscosity η_2, underlain by a viscoelastic half-space with free viscosity η_3. In this Earth model the thickness of the upper crust is equal to the value inferred by *Bills et al.* [1994] for their quasi-elastic crust. Hence the inferred viscosities beneath the upper crust can directly be compared with the results of *Bills et al.* [1994]. Small misfits ($\epsilon < 16$) occur for $\eta_2 \geq 4 \times 10^{19}$ Pa s and $\eta_3 = 10^{18}$ Pa s (Figure 10). All models with $\eta_2 \geq 10^{20}$ Pa s fit the leveling data within the confidence limit, indicating that this value is a lower bound for the viscosity in the lower crust (10-30 km depth). Hence the lower crustal viscosity of 10^{21} Pa s suggested by *Bills et al.* [1994] is consistent with the Lake Mead data. The viscosity of 10^{18} Pa s for subcrustal depth (>30 km) found with model M3a agrees well with the values found in sections 5.1 and 5.2.

This viscosity model with $h_1 = 10$ km, $h_2 = 20$ km, $\eta_2 = 10^{20}$ Pa s, and $\eta_3 = 10^{18}$ Pa s is used as an a priori model for the inverse procedure (Figure 11). The misfit is reduced only slightly from $\epsilon = 12.5$ to 12.0. The resulting viscosity

Table 3. Parameters of Three-Layer Earth Models

Model	Layer	Viscosity η, Pa s	Thickness h, km
M3a	upper crust	∞	$h_1 = 10$
	lower crust	$\eta_2 \in [10^{17}, 10^{23}]$	$h_2 = 20$
	subcrust	$\eta_3 \in [10^{17}, 10^{20}]$	∞
M3b	crust	∞	$h_1 = 30$
	subcrust	$\eta_2 = 10^{18}$	$h_2 \in [50, 400]$
		$\eta_3 \in [10^{17}, 10^{21}]$	∞

Earth models are calculated every 50 km for h_2, and two per decade for η_2 and η_3, resulting in 65 models for M3a and 72 models for M3b.
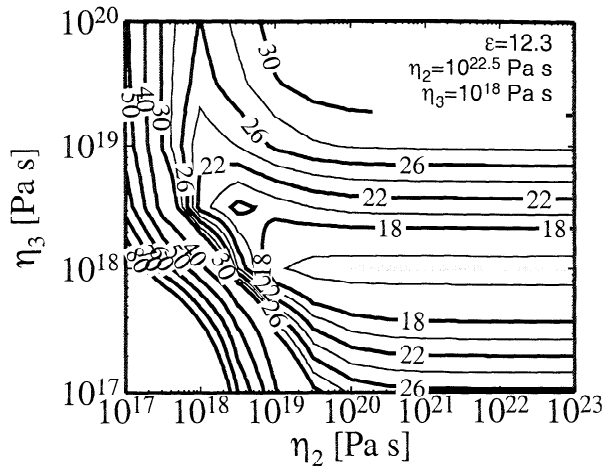
Figure 10. Misfit between observed and modeled deformation for three-layer Earth model M3a as a function of lower crustal viscosity η_2 and subcrustal viscosity η_3. The data used are the same as in Figure 5.

profile is characterized by a high-viscosity upper crust (0-10 km), intermediate viscosities around 2×10^{20} Pa s for the lower crust (10-30 km), and a low-viscosity subcrust (> 30 km). The viscosity profile in the subcrust is similar to the profile resulting from the inversion based on the best fitting two-layer model as a priori model (Figure 7). The ratio of prior to posterior viscosity uncertainties is also similar to the previous inversion (Figure 7), indicating that the subcrustal viscosities are a robust feature of the inversions.

The difference in lower crustal viscosity (10-30 km) obtained using the best fitting two-layer and three-layer models as a priori models for the inversion is significant. It reveals that the leveling data can be explained equally well with an elastic or a viscoelastic lower crust (10-30 km) if the viscosity in the lower crust is larger than 10^{20} Pa s. The lower crust appears quasi-elastic due to the short timescale of subsidence of 25 years. However, the strength relaxes on timescales of 10,000 years and longer, as observed with the Lake Bonneville data. Our rheological model derived from short-term reservoir loading is also consistent with models for long-term loading such as the growth of faults through repeated earthquakes [e.g., *King et al.*, 1988; *Stein et al.*, 1988; *Armijo et al.*, 1996]. Substituting in these models the elastic plate overlying an inviscid half-space by a two-layer elastic-viscoelastic plate would eliminate the need to reduce the seismically inferred shear modulus in the plate to long-term values reduced by factors of 100-1000. The viscoelastic lower crust would account for the required relaxation of the shear modulus.

Viscosities of the order of 10^{18} to 10^{20} Pa s for the lower crust (below a more rigid upper crust of around 10 km thickness) have been inferred from numerical modeling of channel flow induced by topographical loads such as lithospheric extension of the Basin and Range Province (*Kruse et al.* [1991], for the Lake Mead region, and *Kaufman and Royden* [1994], for the Halloran Hills region west of Lake Mead). While topographical loading is on a much longer timescale

of the order of millions of years, it is interesting to note that the upper bounds on viscosities within the lower crust agree within 1 order of magnitude with the results of this study. It is also interesting that the inferred 30-km-thick elastic crust is in agreement with the 35-km value based on seismic surface waves and refraction data [*Priestley et al.*, 1980]. This may indicate that the seismic and rheologic structure of the crust is related.

6.2. Postglacial Rebound

The deformation induced by the growth and the melting of large ice sheets during the last glacial cycles also has been used to infer the viscosity of the upper and lower mantle [e.g., *Lambeck et al.*, 1996; *Mitrovica*, 1996; *Mitrovica and Forte*, 1997; *Lambeck et al.*, 1998]. Most authors agree that the average upper mantle viscosity is around 4×10^{20} Pa s [e.g. *Lambeck et al.*, 1998]. Although this is 1-2 orders of magnitude larger than our estimate of subcrustal viscosity of 10^{18} Pa s, the estimates are consistent: The rebound-inferred value represents an average over the upper mantle (60-660 km depth), whereas the viscosity inferred in this study averages over shallower depths (60-200 km). To demonstrate this, we introduce a three-layer Earth model M3b (Table 3) with an elastic crust of thickness $h_1 = 30$ km, a viscoelastic subcrustal layer of thickness h_2, and viscosity η_2, underlain by a viscoelastic half-space with viscosity η_3. In this model, η_2 is fixed to 10^{18} Pa s, and the free parameters are h_2 and η_3. We will determine the minimum thickness of layer two, h_2, for which the misfit is independent from η_3. This thickness is the resolution depth of the Lake Mead data.

The misfit for Earth model M3b (Figure 12) varies significantly with η_3 for $h_2 < 200$ km but is almost independent of η_3 for $h_2 > 200$ km. This indicates that the
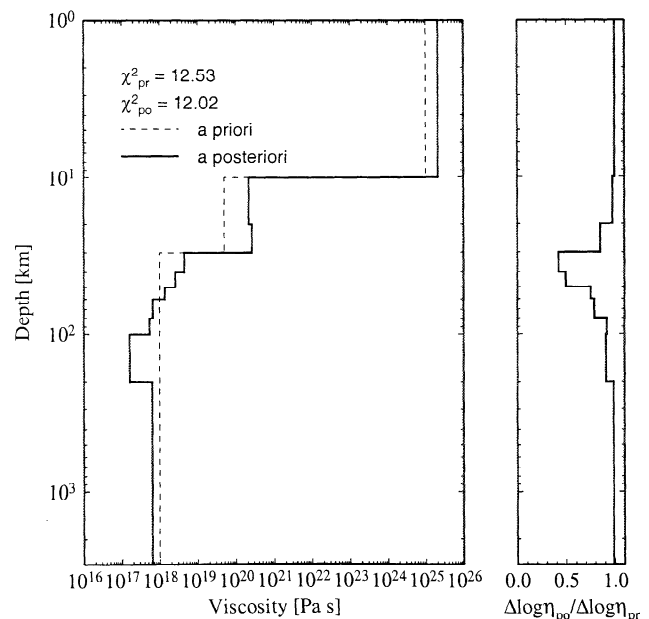

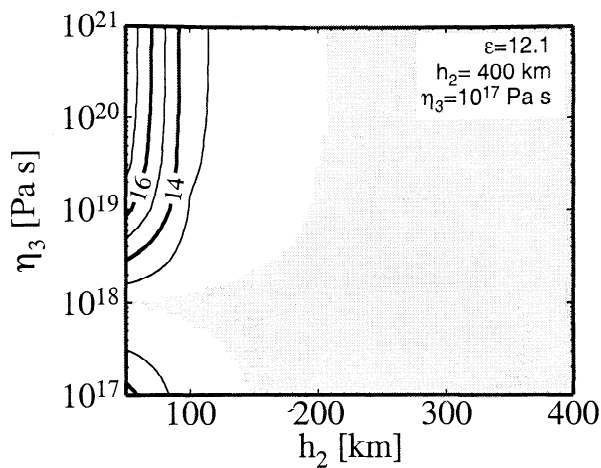**Figure 11.** Same as Figure 7, but using the a priori model inferred from three-layer forward modeling (see Figure 10).

Figure 12. Misfit between observed and modeled deformation for three-layer Earth model M3b as a function of subcrustal thickness h_2 and subcrustal viscosity η_3. The data used are the same as in Figure 5.

leveling data do not constrain η_3 below 200 km depth, as it can also be seen by the large confidence limits. Hence the leveling data agree with viscosities of 10^{18} Pa s above 200 km and 4×10^{20} Pa s below 200 km. Thus, in comparison to postglacial rebound studies, relatively low viscosities in the uppermost mantle (30-200 km) can possibly be attributed to peculiarities of the Basin and Range Province such as high heat flow [Lachenbruch, 1978], recent volcanism [Oviatt and Nash, 1989], and extensional tectonics [Zoback, 1989]. Additionally, the faults of the Basin and Range Province may have deep roots, which may control the deformation. Hence the low subcrustal viscosities based on a Maxwell-viscoelastic continuum model may, in fact, reflect more localized deformation, with strength orders of magnitudes lower than the surrounding solid rock [e.g., Vissers et al., 1995].

6.3. Postseismic Deformation

The relaxation time of ~25 years for the subsidence following the filling of the Lake Mead Reservoir is consistent with relaxation times of 30 and 36 ± 16 years observed for postseismic deformation following large Californian earthquakes [Thatcher, 1983; Kenner and Segall, 2000]. If regional variations in rheology are moderate, we would expect such an agreement because Lake Mead has a spatial extent similar to large earthquakes, and therefore both loads should be sensible to similar subcrustal depths.

We now compare in more detail the viscosity structure derived from the Lake Mead data with those derived from postseismic observations. Pollitz and Sacks [1992] used trilateration data following the 1857 Fort Tejon, California, earthquake to derive a subcrustal viscosity of $4\text{-}8 \times 10^{19}$ Pa s under southern California (>33 km depth). Pollitz and Sacks [1995] used leveling data surveyed after the 1891 Nobi, Japan, earthquake to infer a subcrustal viscosity of 2×10^{19} Pa s under central Honshu (33-163 km depth). Although these estimates are ~1 order of magnitude larger than the subcrustal viscosity of 10^{18} Pa s (>30 km depth) of the

best fitting models for the Lake Mead data, we consider these different estimates to be largely consistent because the resolution of the postseismic data is limited. Details of the load (the earthquake slip distribution) are not well known, and postseismic relaxation may be confused with afterslip. Recently, it was shown that the ground deformation following the 1992 Landers, California, earthquake was caused by viscous relaxation of earthquake-induced stresses and not by afterslip [Deng et al., 1998; Pollitz et al., 1999]. Our result of a subcrustal viscosity of 10^{18} Pa s for the Lake Mead area is largely consistent with the Pollitz et al. [1999] estimate of $8 \pm 4 \times 10^{18}$ Pa s for the uppermost mantle (>30 km) in the Landers area ~200 km to the west of Lake Mead. It is not consistent with the Deng et al. [1998] viscosity inference of 10^{18} Pa s for the lower crust (15-25 km), which is based on the assumption of a subcrustal viscosity of 10^{20} Pa s. If the rheologic structure of the Lake Mead region applies to strike-slip regions like California, then our data favor the Thatcher [1990] thick lithosphere model where the upper crustal fault is loaded by a screw dislocation in the elastic lower crust versus the thin lithosphere model where the fault is loaded by distributed deformation in the lower crust.

6.4. Deformation After 1950

To illustrate the relaxation process, Figure 13 shows the modeled subsidence for the locations Boulder Wash tide gage, Pierce Ferry tide gage, and Cane Springs as a function of time, starting from the filling of the lake in 1935. Cane Springs is located ~100 km from the center of the load, Pierce Ferry is at the margin, and Boulder Wash is close to the center of the load (see Figure 4 for locations). All locations experienced monotonic subsidence after the filling of the lake. The isostatic equilibrium was reached ~1980, when the load-induced stresses in the subcrust were relaxed. In 1950, the time of the third leveling survey, the predicted subsidence already reached 75% of the final isostatic equilibrium. This explains that the leveling in 1963 does not differ much from the 1950 survey. In fact, the model predicts that <25% of the total subsidence occurs after 1950. Hence other effects, such as the seasonal variation in lake
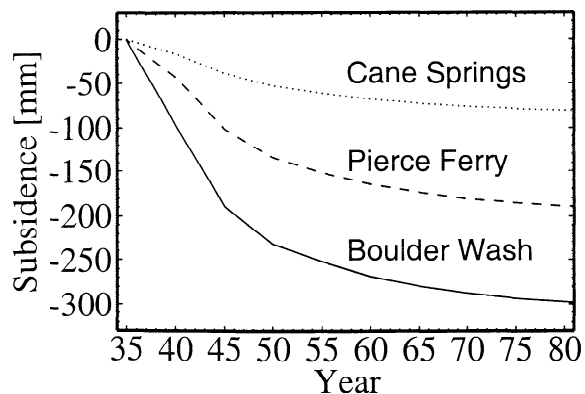

Figure 13. Modeled subsidence for Earth model M2 with $h_1 = 30$ km and $\eta_2 = 10^{18}$ Pa s for locations Boulder Wash, Pierce Ferry, and Cane Springs.

level with its instantaneous elastic response of the basement, become more important from this time on.

7. Conclusions

The surface deformation induced by the water load of the Lake Mead reservoir can be explained by viscous relaxation beneath the elastic crust. The observations of three leveling surveys are best explained using an Earth model with an elastic crust of 30 ± 3 km thickness and a subcrust with a relatively low viscosity of $10^{18\pm0.2}$ Pa s. The result of a 30-km-thick elastic crust may be related to the short timescale of subsidence ($T < 25$ years). We cannot resolve between an elastic and a viscoelastic lower crust with viscosities larger than 10^{20} Pa s. This lower bound of the viscosity for the lower crust is consistent with bounds on the viscosity from topographical loading in the same region. It is also consistent with results from postseismic deformation studies in other regions where the relaxation is assumed to occur in the uppermost mantle. It is in contrast to postseismic studies assuming that the relaxation occurs in the lower crust.

A comparison of our inferred viscosity profile with other viscosity profiles for the Basin and Range Province is shown in Figure 14. In general, our profile is consistent with previously published results. The leveling data also indicate a gradually decreasing viscosity in the subcrust from 10^{19} to 10^{18} Pa s (30-200 km), but this viscosity decrease is not a robust result of the inversion. The Lake Mead subsidence data constrain the viscosity profile to 200 km depth.
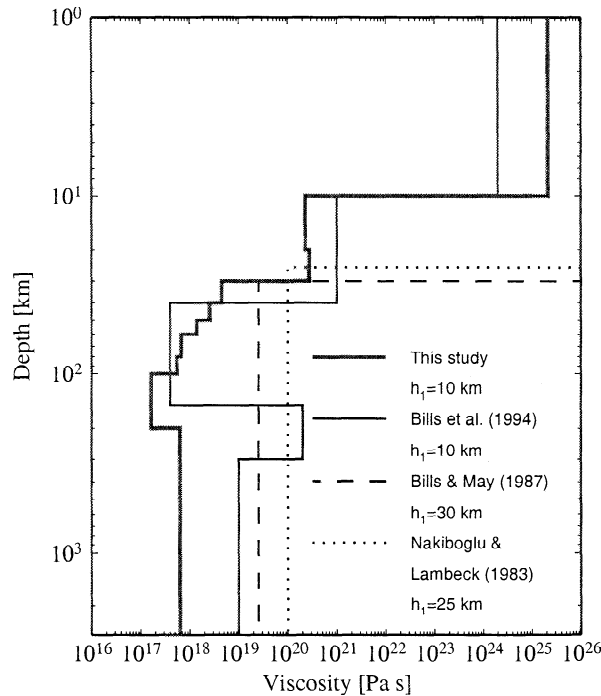

Figure 14. Comparison of different viscosity profiles in the Basin and Range Province. The numbers in the legend are crustal thickness estimates.

Appendix: Elements of Rheology and Propagator Matrices

$$
\begin{aligned}
M_{11} &= 0, & M_{12} &= k, \\
M_{13} &= \tfrac{1}{\mu}, & M_{14} &= 0, \\
M_{21} &= -\frac{\lambda k}{\lambda + 2\mu}, & M_{22} &= 0, \\
M_{23} &= 0, & M_{24} &= \frac{1}{\lambda + 2\mu}, \\
M_{31} &= 4\mu k^2 \frac{\lambda + \mu}{\lambda + 2\mu}, & M_{32} &= \rho g k, \\
M_{33} &= 0, & M_{34} &= \frac{\lambda k}{\lambda + 2\mu}, \\
M_{41} &= \rho g \frac{\lambda k}{\lambda + 2\mu}, & M_{42} &= 0, \\
M_{43} &= -k, & M_{44} &= -\rho g \frac{1}{\lambda + 2\mu}.
\end{aligned}
\tag{A1}
$$

$$P_{11} = Ass + ch, \tag{A2a}$$
$$P_{12} = -(Acc + Bsh) + ss\rho g/(2\mu k), \tag{A2b}$$
$$P_{13} = -(Acc + Csh)/(2\mu k), \tag{A2c}$$
$$P_{14} = Ass/(2\mu k), \tag{A2d}$$
$$P_{21} = Acc - Bsh, \tag{A2e}$$
$$P_{22} = -Ass + ch + (cc - sh)\rho g/(2\mu k), \tag{A2f}$$
$$P_{23} = -Ass/(2\mu k), \tag{A2g}$$
$$P_{24} = (Acc - Csh)/(2\mu k), \tag{A2h}$$
$$P_{31} = -A(cc + sh)(2\mu k), \tag{A2i}$$
$$P_{32} = Ass(2\mu k) - cc\rho g, \tag{A2j}$$
$$P_{33} = Ass + ch, \tag{A2k}$$
$$P_{34} = -Acc + Bsh, \tag{A2l}$$
$$P_{41} = -Ass(2\mu k) - cc\rho g, \tag{A2m}$$
$$P_{42} = A(cc-sh)(2\mu k) - (cc - sh)(\rho g)^2/(2\mu k), \tag{A2n}$$
$$P_{43} = Acc + Bsh + ss\rho g/(2\mu k), \tag{A2o}$$
$$P_{44} = -Ass + ch - (cc - sh)\rho g/(2\mu k), \tag{A2p}$$

where

$$sh = \sinh(kh), \tag{A3a}$$
$$ch = \cosh(kh), \tag{A3b}$$
$$ss = kh\sinh(kh), \tag{A3c}$$
$$cc = kh\cosh(kh), \tag{A3d}$$
$$A = \frac{\lambda + \mu}{\lambda + 2\mu}, \tag{A3e}$$
$$B = \frac{\mu}{\lambda + 2\mu}, \tag{A3f}$$
$$C = \frac{\lambda + 3\mu}{\lambda + 2\mu}. \tag{A3g}$$

References

Amelung, F., D. L. Galloway, J. W. Bell, H. A. Zebker, and R. J. Laczniak, Sensing the ups and downs of Las Vegas: InSAR reveals structural control of land subsidence and aquifer-system deformation, *Geology, 27*(6), 483–486, 1999.

Armijo, R., B. Meyer, G. C. P. King, A. Rigo, and D. Papanastassiou, Quarternary evolution of the Corinth Rift and its implications for the Late Cenozoic evolution of the Aegean, *Geophys. J. Int., 126*, 11–53, 1996.

Arnadottir, T., P. Segall, and M. Matthews, Resolving the discrepancy between geodetic and seismic fault models for the 1989 Loma Prieta, California, earthquake, *Bull. Seismol. Soc. Am., 82*(5), 2248–2255, 1992.

Bills, B. G. and G. M. May, Lake Bonneville: Constraints on lithospheric thickness and upper mantle viscosity from isostatic warping of Bonneville, Provo, and Gilbert stage shorelines, *J. Geophys. Res., 92*(B11), 11,493–11,508, 1987.

Bills, B. G., D. R. Currey, and G. A. Marshall, Viscosity estimates for the crust and upper mantle from patterns of lacust shoreline deformation in the Eastern Great Basin, *J. Geophys. Res., 99*(B11), 22,059–22,086, 1994.

Biot, M. A., Mechanics of deformation and acoustic propagation in porous media, *J. Appl. Phys., 33*, 1482–1498, 1962.

Brace, W. F., and D. L. Kohlstedt, Limits of lithospheric stress imposed by laboratory experiments, *J. Geophys. Res., 85*(11), 6248–6252, 1980.

Breuer, D., and D. Wolf, Deglacial land emergence and lateral upper–mantle heterogeneity in the Svalbard Archipelago, I, first results for simple load models, *Geophys. J. Int., 121*, 775–788, 1995.

Buergmann, R., P. Segall, M. Lisowski, and J. L. Svarc, Postseismic strain following the Loma Prieta earthquake from repeated GPS measurements, in *The Loma Prieta, California, Earthquake of October 17, 1989*, edited by P. A. Reasenberg, *U.S. Geol. Surv. Prof. Pap., 1558*, 209–244, 1997.

Burov, E. B., and M. Diament, The effective elastic thickness (t_e) of continental lithosphere: What does it really mean?, *J. Geophys. Res., 100*(B3), 3905–3927, 1995.

Carder, D. S., and J. B. Small, Level divergences, seismic activity, and reservoir loading in the Lake Mead area, Nevada and Arizona, *Eos Trans. AGU, 29*(6), 767–771, 1948.

Deng, J., M. Gurnis, H. Kanamori and E. Hauksson, Viscoelastic flow in the lower crust after the 1992 Landers, California, earthquake, *Science, 282*, 1689–1692, 1998.

Goetze, C., and B. Evans, Stress and temperature in the bending lithosphere as constrained by experimental rock mechanics, *Geophys. J. R. Astron. Soc., 59*(3), 463–478, 1979.

Gould, H. R., Amount of sediment, in *Comprehensive Survey of Sedimentation in Lake Mead, 1948–49*, edited by W. O. Smith, C. P. Vetter, and C. B. Cummings, *U.S. Geol. Surv. Prof. Pap., 295*, 195–200, 1960.

Heiskanen, W. A., and H. Moritz, *Physical Geodesy*, W. H. Freeman, New York, 1967.

Hodgkinson, K. M., R. S. Stein, and G. Marshall, Geometry of the 1954 Fairview Peak-Dixie Valley earthquake sequence from a joint inversion of leveling and triangulation data, *J. Geophys. Res., 101*(B11), 25,437–25,457, 1996.

Kaufman, P. S., and L. H. Royden, Lower crustal flow in an extensional setting: Constraints from the Halloran Hills region, eastern Mojave desert, California, *J. Geophys. Res., 99*(B8), 15,723–15,739, 1994.

Kenner, S. J., and P. Segall, Postseismic Deformation following the 1906 San Francisco earthquake, *J. Geophys. Res.*, in press, 2000.

King, G. C. P., R. S. Stein, and J. B. Rundle, The growth of geological structures by repeated earthquakes, 1, Conceptual framework, *J. Geophys. Res., 93*(B11), 13,307–13,318, 1988.

Klein, A., W. Jacoby, and P. Smilde, Mining-induced crustal defor-mation in northwest Germany: Modelling the rheological structure of the lithosphere, *Earth Planet. Sci. Lett., 147*, 107–123, 1997.

Kohlstedt, D. L., B. Evans, and S. J. Mackwell, Strength of the lithosphere: Constraints imposed by laboratory experiments, *J. Geophys. Res., 100*(B9), 17,587–17,602, 1995.

Kruse, S., M. McNutt, J. Phipps-Morgan, L. Royden and B. Wernicke, Lithospheric extension near Lake Mead, Nevada: a model for ductile flow in the lower crust, *J. Geophys. Res., 96*(B3), 4435–4456, 1991.

Lachenbruch, A. H., Heat flow in the Basin and Range Province and thermal effects of tectonic extension, *Pure Appl. Geophys., 117*, 34–50, 1978.

Lambeck, K., P. Johnston, C. Smither, and M. Nakada, Glacial rebound of the British Isles, III, Constraints on mantle viscosity, *Geophys. J. Int., 125*, 340–354, 1996.

Lambeck, K., C. Smither, and P. Johnston, Sea-level change, glacial rebound and mantle viscosity for northern Europe, *Geophys. J. Int., 134*, 102–144, 1998.

Langbein, W. B., Water budget, in *Comprehensive Survey of Sedimentation in Lake Mead, 1948–49*, edited by W. O. Smith, C. P. Vetter, and C. B. Cummings, *U.S. Geol. Surv. Prof. Pap., 295*, 95–102, 1960.

Lara, J. M., and J. I. Sanders, The 1963-64 Lake Mead survey, Technical report, Bur. of Reclam., U.S. Dep. of Inter., Washington, D.C., 1970.

Longwell, C. R., Interpretation of the leveling data, in *Comprehensive Survey of Sedimentation in Lake Mead, 1948–49*, edited by W. O. Smith, C. P. Vetter, and C. B. Cummings, *U.S. Geol. Surv. Prof. Pap., 295*, 33–38, 1960a.

Longwell, C. R., Geological setting of Lake Mead, in *Comprehensive Survey of Sedimentation in Lake Mead, 1948–49*, edited by W. O. Smith, C. P. Vetter, and C. B. Cummings, *U.S. Geol. Surv. Prof. Pap., 295*, 11–20, 1960b.

Marshall, G. A., R. S. Stein, and W. Thatcher, Faulting geometry and slip from co-seismic elevation changes: The 18 October 1989, Loma Prieta, California, earthquake, *Bull. Seismol. Soc. Am., 81*(5), 1660–1693, 1991.

Menke, W., *Geophysical Data Analysis: Discrete Inverse Theory*, Academic, San Diego, Calif., 1989.

Mitrovica, J. X., Haskell [1935] revisited, *J. Geophys. Res., 101* (B1), 555–569, 1996.

Mitrovica, J. X., and A. M. Forte, Radial profile of mantle viscosity: Results from a joint inversion of convection and postglacial rebound observables, *J. Geophys. Res., 102*(B2), 2751–2769, 1997.

Mitrovica, J. X., and W. R. Peltier, A comparison of methods for the inversion of viscoelastic relaxation spectra, *Geophys. J. Int., 108*, 410–414, 1992.

Murray, M. H., G. A. Marshall, M. Lisowski, and R. S. Stein, The 1992 M=7 Cape Mendocino, California, earthquake: Coseismic deformation at the south end of the Cascadia megathrust, *J. Geophys. Res., 101*(B8), 17,707–17,725, 1996.

Nakiboglu, S. M., and K. Lambeck, A study to the Earth's response to surface loading with application to Lake Bonneville, *Geophys. J. R. Astron. Soc., 70*, 577–620, 1982.

Nakiboglu, S. M., and K. Lambeck, A reevaluation of the isostatic rebound of Lake Bonneville, *J. Geophys. Res., 88*(B12), 10,439–10,447, 1983.

Oviatt, C. G., and W. P. Nash, Late Pleistocene basaltic ash and volcanic eruptions in the Bonneville Basin, Utah, *Geol. Soc. Am. Bull., 101*, 292–303, 1989.

Parkin, E. J., Precise leveling, in *Comprehensive Survey of Sedimentation in Lake Mead, 1948–49*, edited by W. O. Smith, C. P. Vetter, and C. B. Cummings, *U.S. Geol. Surv. Prof. Pap., 295*, 21–32, 1960.

Passey, Q. R., Upper mantle viscosity derived from the difference in rebound of the Provo and Bonneville shorelines: Lake Bon-

neville basin, Utah, *J. Geophys. Res., 86*(B12), 11,701–11,708, 1981.

Peltier, W. R., The impulse response of a Maxwell Earth, *Rev. Geophys., 12*(4), 649–669, 1974.

Pollitz, F. F., and I. S. Sacks, Modelling of postseismic relaxation following the great 1857 earthquake, southern California, *Bull. Seismol. Soc. Am., 82,* 454–480, 1992.

Pollitz, F. F., and I. S. Sacks, Consequences of stress changes following the 1891 Nobi earthquake, Japan, *Bull. Seismol. Soc. Am., 85,* 796–807, 1995.

Pollitz, F. F., R. Buergmann, and P. Segall, Joint estimation of afterslip rate and postseismic relaxation following the 1989 Loma Prieta earthquake, *J. Geophys. Res., 103*(B11), 26,975–26,992, 1998.

Pollitz, F. F., G. Peltzer, and R. Bürgmann, Mobility of continental mantle: Evidence from postseismic geodetic observations following the 1992 Landers earthquake *J. Geophys. Res., 105*(B4), 8035–8054, 1999.

Priestley, K., J. A. Orcutt, and J. N. Brune, Higher-mode surface waves and structure of the Great Basin of Nevada, and Western Utah, *J. Geophys. Res., 85*(B12), 7166–7174, 1980.

Rogers, A. M., and W. H. K. Lee, Seismic study of earthquakes in the Lake Mead, Nevada-Arizona region, *Bull. Seismol. Soc. Am., 66,* 1657–1681, 1976.

Rydelek, P. A., and I. S. Sacks, Asthenospheric viscosity and stress diffusion: a mechanism to explain correlated earthquakes and surface deformations in NE Japan, *Geophys. J. Int., 100,* 39–58, 1990.

Savage, J. C., Equivalent strike-slip earthquake cycles in half-space and lithosphere-asthenosphere Earth models, *J. Geophys. Res., 95*(B4), 4873–4879, 1990.

Schapery, R. A., Approximate methods of transform inversion for viscoelastic stress analysis, *Proc. U.S. Nat. Congr. Appl. Mech.,* 4th, 1075–1085, 1961.

Smith, W. O., C. P. Vetter, and C. B. Cummings (Eds.), *Comprehensive survey of sedimentation in Lake Mead, 1948–49, U.S. Geol. Surv. Prof. Pap., 295,* 1960.

Snieder, R., The role of nonlinearity in inverse problems, *Inverse Problems, 14*(3), 387–404, 1998.

Solling, A. D., Geoid deformation in Hoover Dam Area, *J. Coast Geod. Surv., 3,* 102–104, 1950.

Stanley, J. W., Reservoir storage, in *Comprehensive Survey of Sedimentation in Lake Mead, 1948–49,* edited by W. O. Smith, C. P. Vetter, and C. B. Cummings, *U.S. Geol. Surv. Prof. Pap., 295,* 83–93, 1960.

Stein, R. S., Discrimination of tectonic displacement from slope-dependent errors in geodetic leveling from Southern California, 1953-1979, in *Earthquake Prediction: An International Review,*

Maurice Ewing Ser., Vol. 4, edited by D. W. Simpson and P. G. Richards, pp. 441–456, AGU, Washington, D.C., 1981.

Stein, R. S., G. C. P. King, and J. B. Rundle, The growth of geological structures by repeated earthquakes 2. Field examples of continental dip-slip faults, *J. Geophys. Res., 93*(B11), 13,319–13,331, 1988.

Taibai, T., Crustal movements in the inner zone of southwest Japan associated with stress relaxation after major earthquakes, *J. Phys. Earth, 37,* 101–131, 1989.

Tarantola, A., and B. Valette, Generalized nonlinear inverse problems solved using the least squares criterion, *Rev. Geophys., 20*(2), 219–232, 1982.

Thatcher, W., Nonlinear strain buildup and the earthquake cycle on the San Andreas Fault, *J. Geophys. Res., 88*(B7), 5893–5902, 1983.

Thatcher, W., Present-day crustal movements and the mechanics of cyclic deformation, in: *The San Andreas Fault System,* edited by R.E. Wallace, *U.S. Geol. Surv. Prof. Pap., 1515,* 189-206, 1990.

Thatcher, W., T. Matsuda, T. Kato, and J. B. Rundle, Lithospheric loading by the 1896 Riki-u earthquake, northern Japan: Implications for plate flexure and asthenospheric rheology, *J. Geophys. Res., 85*(B11), 6429–6435, 1980.

Turcotte, D. L., and G. Schubert, *Geodynamics,* John Wiley, New York, 1982.

Vissers, R. L. M., M. R. Drury, E. H. Hoogerduijn Strating, C. J. Spiers and D. van der Wal, Mantle shear zones and their effect on lithosphere strength during continental breakup, *Tectonophysics, 249,* 155–171, 1995.

Ward, S. N., Quasi-static propagator matrices: creep on strike-slip faults, *Tectonophysics, 120,* 83–106, 1985.

Wessel, P., and W. H. F. Smith, Free software helps map and display data, *Eos Trans. AGU, 72,* 441, 445–446, 1991.

Wolf, D., The normal modes of a layered, incompressible Maxwell half-space, *J. Geophys., 57,* 106–117, 1985a.

Wolf, D., On deglaciation–induced perturbations of the geoid, *Can. J. Earth Sci., 23,* 269–272, 1985b.

Zoback, M. L., State of stress and modern deformation in the northern Basin and Range Province, *J. Geophys. Res., 94*(B6), 7105–7128, 1989.

G. Kaufmann, Institut für Geophysik, Universität Göttingen, D-37075 Göttingen, Germany. (gkaufman@uni-geophys.gwdg.de)

F. Amelung, HIGP/SOEST, University of Hawaii, 2525 Correa Road, Honolulu, HI, 96822. (amelung@pgd.hawaii.edu)